Higgs and Goldstone spin-wave modes in striped magnetic texture

Matías Grassi [1], Moritz Geilen,[2] Kosseila Ait Oukaci [3], Yves Henry [1], Daniel Lacour [3], Daniel Stoeffler [1], Michel Hehn [3], Philipp Pirro [2], and Matthieu Bailleul [1]

[1]*Université de Strasbourg, CNRS, Institut de Physique et Chimie des Matériaux de Strasbourg, UMR 7504, F-67000 Strasbourg, France*
[2]*Fachbereich Physik and Landesforschungszentrum OPTIMAS, Technische Universität Kaiserslautern, D-67663 Kaiserslautern, Germany*
[3]*Institut Jean Lamour, Université de Lorraine, UMR 7198, CNRS, F-54000 Nancy, France*

Spontaneous symmetry breaking is ubiquitous in physics. Its spectroscopic signature consists in the softening of a specific mode upon approaching the transition from the high-symmetry side and its subsequent splitting into a zero-frequency Goldstone mode and a nonzero-frequency Higgs mode. Although they determine the whole system dynamics, these features are difficult to address in practice because of their vanishing coupling to most experimental probes and/or their strong interaction with other fluctuations. In this paper, we consider a periodic magnetic modulation occurring in a ferromagnetic film with perpendicular-to-plane magnetic anisotropy and observe its Goldstone and Higgs spin-wave modes at room temperature using microwave and optical techniques. This simple system constitutes a particularly convenient platform for further exploring the dynamics of symmetry breaking.

I. INTRODUCTION

Upon spontaneous symmetry breaking, a system organizes itself in a state with a lower symmetry than that of its constituting entities, as exemplified by superconducting, magnetic, or incommensurate structural phases [1,2]. According to the Landau theory, such a transition is conveniently visualized by defining an order parameter ψ and following the morphology of the free-energy surface $E(\psi)$ [3]. This is illustrated in Fig. 1(a) for a system with $U(1)$ symmetry, where ψ is a complex number (or, equivalently, a two-dimensional real vector). In the high-symmetry phase, E presents a single minimum at $\psi = 0$. Upon driving the system through the transition, the curvature around this point decreases, reaches zero at the critical point, and then changes sign. In the low-symmetry phase, the energy surface eventually takes the shape of a Mexican hat with a degenerate minimum extending over a circle of radius $|\psi| = \psi_0$. The system has to "choose" a phase $\arg(\psi)$, which constitutes the symmetry break. This particular energy landscape gives rise to characteristic low-frequency dynamic modes, conveniently viewed as the oscillations of a mass moving on such a surface [1]. Upon driving the system from the high-symmetry phase, the oscillations around the $\psi = 0$ minimum [blue arrow in Fig. 1(a)] are expected to soften gradually, reach zero frequency at the critical point, and subsequently split in two, a zero-frequency mode with azimuthal trajectory along the rim and a nonzero-frequency mode with radial trajectory across the rim [solid and dashed red arrows in Fig. 1(a), respectively]. These two modes, referred to as Goldstone and Higgs modes, respectively, dominate the whole dynamics of the low-symmetry phase, but also its coupling to external degrees of freedom, in particular, gauge ones. Originally explored in the context of superconductivity, the latter is of particular importance for particle physics, as the

finite masses of the W and Z weak bosons can only be explained by their coupling to the symmetry-breaking Higgs field [4,5].

Although these dynamics are of crucial interest, their direct observation is a serious challenge as it requires driving the system through the transition while keeping experimental access to the relevant low-frequency excitations, particularly prone to overdamping due to defects and thermal/quantum microscopic fluctuations [2,6]. This difficulty could be avoided in low-temperature inelastic neutron scattering studies of very specific pressure-induced structural and magnetic transitions [7,8]. More recently, it was proposed to use artificial systems, namely ultracold boson lattices, which can be driven through a quantum phase transition, their excitations being characterized via real-time optical spectroscopy [9,10].

In this paper, we show that an archetypal system of micromagnetism, the so-called magnetic weak stripes, allows for a room-temperature observation of the Higgs/Goldstone dynamics by inelastic light scattering and microwave spectroscopy. Magnetic weak stripes consist of a field-tunable modulation at a mesoscopic scale occurring in ferromagnetic films possessing a moderate perpendicular magnetic anisotropy [11]. The stability of this texture was predicted in the early days of theoretical micromagnetism [3,12–14], and later confirmed by static magnetic imaging [15,16]. Several studies have explored the corresponding dynamics evidencing a complex set of vibration modes varying to a very large extent with the magnetic parameters of the film and upon application of a control magnetic field. Initially described within local resonance models (domain/domain-wall resonance) [17–19], this complex phenomenology has recently been rephrased in the vocabulary of magnonics, as a complex set of spin-wave modes localized/scattered by the periodic

094444-1
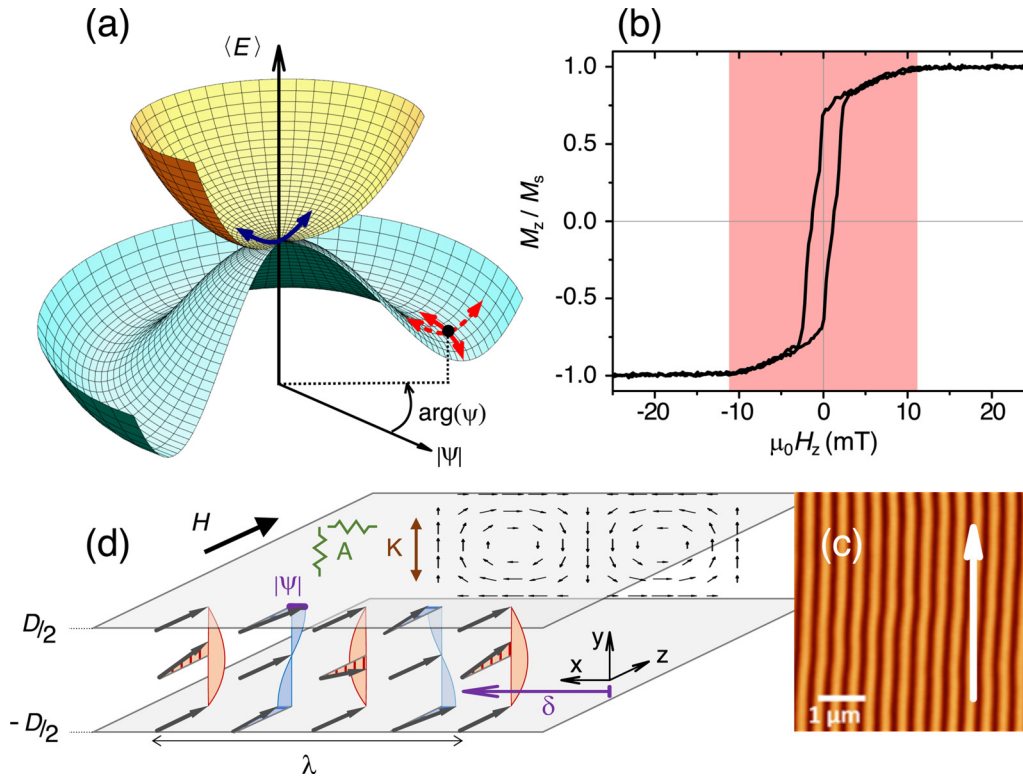
FIG. 1. (a) Sketch of the characteristic dynamic modes associated with $U(1)$ symmetry breaking. The blue arrow shows the degenerate modes in the high-symmetry phase (yellow potential surface). The solid and dashed red arrows show the Goldstone and Higgs modes in the low-symmetry phase (sombrero-shaped blue potential surface). (b) Magnetization loop measured for our 180-nm $Co_{40}Fe_{40}B_{20}$ film with a magnetic field H in the plane. (c) Magnetic force microscopy image of the weak stripe magnetic texture existing below the critical field H_c (shown here at remanence). The white arrow shows the direction of the previously applied field. (d) Sketch of the three-dimensional normalized magnetization distribution $M(x, y, z)/M_S$ within the weak stripe texture, together with its minimal description in terms of a $U(1)$ symmetry breaking, with associated amplitude $|\psi|$ and phase $\arg(\psi) = k\,\delta$ (see details in the text).

modulation [20–22]. Moving ahead in that direction, we provide here a unified description of both statics and dynamics of magnetic stripes based on the identification of a specific spin-wave mode which, upon stripe nucleation, softens and then splits into a Goldstone/Higgs pair. For this purpose, we first formulate an elementary analytical model of the stripe statics and related spin-wave dynamics based on the Landau theory of phase transitions. Then, we report inelastic light scattering measurements conducted down to spin-wave wavelength of the order of the modulation period for different points across the critical region. Confronting them with complementary ferromagnetic resonance measurements and micromagnetic simulations, we arrive at a global picture of the low-frequency dynamics related to such symmetry breaking.

II. RESULTS

The system studied consists of an amorphous $Co_{40}Fe_{40}B_{20}$ film of thickness $D = 180$ nm deposited on intrinsic silicon and initialized by applying a saturating magnetic field H in the film plane. Upon reducing the magnitude of the field below about 12 mT, the average magnetization of the film starts to decrease in a roughly linear fashion [Fig. 1(b)]. In this regime, magnetic force microscopy allows one to identify a modulation periodic in one dimension with a wave number of about $2\pi/(300 \text{ nm}) = 21$ rad/μm [Fig. 1(c)] [23], identified

with the archetypical magnetic weak stripes arising in films which possess a moderate perpendicular magnetic anisotropy K [11]. In the following, we shall revisit this texture from the point of view of its dynamics. For this purpose, we start by describing a minimal model for stripe nucleation, as sketched in Fig. 1(d). The mechanism consists of a competition between the in-plane magnetic field H, which tends to maximize the component of the magnetization distribution $M(x, y)$ along its direction $\hat{z}$ (the system is assumed to be invariant along z), and the perpendicular magnetic anisotropy, which tends to maximize its (out-of-plane) y component. The inhomogeneity of the texture is induced by the dipolar interaction. In order to avoid the large demagnetizing energy density that would be associated with a uniform out-of-plane excursion of magnetization ($\frac{\mu_0}{2}M_y^2$, μ_0 being the permeability of vacuum), the latter favors an alternation of sign of M_y in the film interior, along the transverse direction x, together with a closure of the resulting magnetic flux via quadrature sign changes of the transverse component M_x at both film surfaces. Finally, the overall distribution is smoothed out by the exchange energy density $A\nabla^2 M$, where A is the exchange stiffness constant. For the magnetic parameters of our film ($M_S = 1330$ kA/m, $K = 32.7$ kJ/m^3, $A = 16.6$ pJ/m) [24–27] the comparison of the different energy scales deduced from a dimensional analysis $\mu_0 M_S^2 \gg K \sim \frac{A}{D^2}$ suggests the use of a stray-field-free ansatz of the magnetization distribution, which cancels the

dominant demagnetizing energy while reducing the magnetic anisotropy contribution with respect to an in-plane saturated state. Following Hubert [28], we write this ansatz as a combination of two sinusoidal functions in quadrature with each other:

$$\frac{\boldsymbol{M}}{M_S}(x, y) = |\psi| \left\{ \sin[k(x-\delta)] \sin\left(\frac{\pi y}{D}\right) \hat{\boldsymbol{x}} \right.$$
$$\left. + \frac{kD}{\pi} \cos[k(x-\delta)] \cos\left(\frac{\pi y}{D}\right) \hat{\boldsymbol{y}} \right\}. \quad (1)$$

This ensures the vanishing of both surface magnetic charges $[M_y(y = \pm D/2) = 0]$ and volume magnetic charges $(\frac{\partial M_x}{\partial x} + \frac{\partial M_y}{\partial y} = 0)$. Here, k is the wave number of the modulation ($k = 2\pi/\lambda$ for which we will select later the value minimizing the total energy). With the two other parameters defining the modulation, namely its amplitude $|\psi|$ (taken as the maximum in-plane excursion of the magnetization) and its lateral positioning δ [measured with respect to an arbitrary reference point—see Fig. 1(d)], we build a complex number $\psi = |\psi| e^{ik\delta}$ that we identify with the order parameter of the stripe texture. Then, following Landau theory [3], we develop the spatially averaged magnetic energy density $\langle E \rangle = E_0 + a(k, H)|\psi|^2 + b(k, H)|\psi|^4 + O(|\psi|^6)$, the terms with odd powers being zero by symmetry (see Supplemental Material [24] and Refs. [29,30] therein for details). This simple form allows us to derive an analytical estimate of the field and wave number at the critical point ($\mu_0 H_c = \frac{2K}{M_S} - \frac{4\pi\sqrt{AK}}{DM_S} = 10.5$ mT, $k_c = \frac{\pi}{D}\sqrt{\frac{2K+\mu_0 M_S H_c}{2K-\mu_0 M_S H_c}} = 21.6$ rad/μm, respectively, as deduced from the conditions $a = \frac{\partial a}{\partial k} = 0$), and the modulation amplitude below nucleation $\psi_0 = \sqrt{\frac{-a(k_c, H)}{2b(k_c, H)}}$. Despite its simplicity, this explicit model captures most of the physics of the weak stripes observed experimentally. Despite a small underestimate of critical field of 1.3 mT, it is also in good agreement with micromagnetic simulations [24].

Our minimal model of stripe nucleation forms the skeleton of a description of the spin-wave dynamics in this regime: We place ourselves in the saturated state and consider a plane wave of angular frequency ω and wave number k propagating along $\hat{\boldsymbol{x}}$, $\boldsymbol{m}(y) e^{i(\omega t - kx)}$ [spin-wave configuration referred to as Damon-Eshbach, Fig. 2(a)] [34]. Its complex amplitude distribution $\boldsymbol{m}(y)$ is written as a linear combination of four vector functions: the two functions $\sin(\pi y/D)\hat{\boldsymbol{x}}$ and $\cos(\pi y/D)\hat{\boldsymbol{y}}$ appearing in the static ansatz of Eq. (1) and two extra ones $\sin(\pi y/D)\hat{\boldsymbol{y}}$ and $\cos(\pi y/D)\hat{\boldsymbol{x}}$ obtained through a local 90° rotation and necessary for describing the precession of the magnetization. Unlike the former, the latter pair of functions carries magnetic pseudocharges [Fig. 2(a)], so that the precession will lead to sizable stray fields. We identify the associated demagnetizing energy with a kinetic energy, which, combined with the potential energy $\langle E \rangle$ described above, will determine the mode frequency, in analogy with the Döring mass term of magnetic domain-wall dynamics [11]. More specifically, we shall project the linearized equation of motion of the magnetization, $i\omega \boldsymbol{m} = \gamma M_S \hat{\boldsymbol{z}} \times \frac{\partial E}{\partial \boldsymbol{m}}$, where γ is the gyromagnetic ratio, onto this basis set and diagonalize the resulting 4×4 matrix [Eq. (S9)] to obtain eigenfrequencies and eigenmodes [35]. The spin-wave dispersion relation $\omega(k)/(2\pi)$ obtained for the lowest-frequency mode is shown in the top
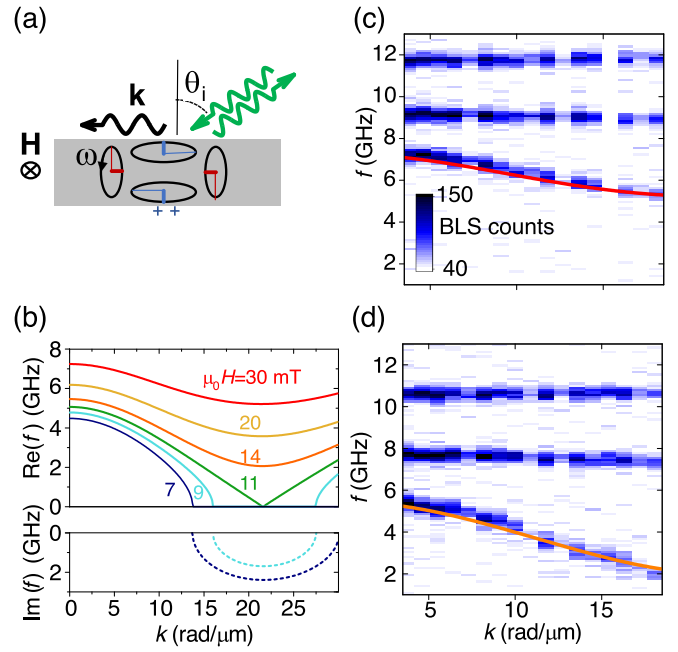
FIG. 2. (a) Sketch of the Damon-Eshbach geometry, magnetization precession (black ellipses), and basis functions used for modeling (red and blue bars). The thin bars can be combined to form the stray-field-free ansatz of Eq. (1), while the thick bars, orthogonal to them, carry nonzero magnetic pseudocharges, as shown at the bottom of the film. (b) Spin-wave dispersion relations calculated analytically using the basis of (a) (see details in the text and Refs. [24,31–33]), for an external field of 30, 20, 14, 11, 9, and 7 mT. For the last two values, the saturated state is unstable, and the spin-wave frequency becomes imaginary over a certain range of wave numbers (see the distinct vertical scale at the bottom of the graph). (c), (d) Color maps of the Brillouin light scattering intensity measured as function of the transferred wave vector [scattering geometry shown by the green arrows in (a)] and transferred frequency f under an external field of $\mu_0 H = 30$ and 14 mT, respectively. The lines show the calculated soft mode frequency [same as in (b)].

panel of Fig. 2(b) for different values of the applied field. Far above nucleation, one distinguishes clearly a nonmonotonic wave-vector dependence with a minimum frequency at a nonzero wave vector of about 21 rad/μm. This minimum constitutes the dynamic precursor of stripe nucleation: Its wave number is the critical one k_c of the stripe modulation and its frequency tends to zero as H approaches H_c. This allows us to reinterpret stripe domain nucleation as the freezing of the lowest-frequency spin wave of the system [36].

To observe this characteristic mode softening, we now resort to Brillouin light scattering (BLS), an inelastic light scattering technique capable of probing thermally excited spin waves over a broad range of wave vectors. The measurement geometry is sketched in Fig. 2(a): The film is illuminated with a laser beam under an angle of incidence θ_i in the presence of a magnetic field $\boldsymbol{H}$ perpendicular to the incidence plane. The backscattered light is collected and frequency analyzed with a high finesse Fabry-Pérot interferometer. Due to the conservation of energy and in-plane linear momentum, the frequency shift of the scattered light and the transferred wave vector [$k = 4\pi/\lambda_{\text{laser}} \sin(\theta_i)$] are to be identified with

those of the quasiparticles absorbed/emitted during the scattering process. In our case, these are the spin waves which couple to light via magneto-optical effects [37].

Figure 2(c) shows a color plot of the spectra recorded in the saturated state with $\mu_0 H = 30$ mT for different transferred wave vectors, thus providing a direct picture of the spin-wave dispersions, up to a wave vector of about $k = 18$ rad/μm. One recognizes clearly three spin-wave branches. The two highest ones with nearly constant frequency can be assigned to perpendicular standing spin waves with an increasing number of nodal planes across the film thickness [24,38]. On the other hand, the lowest-frequency branch clearly shows a negative group velocity (frequency decreases as the wave vector increases) for a wave vector above a few rad/m, which fits very well with the dispersion relation calculated for the stripe precursor mode (red line). This negative velocity can appear surprising at first glance since spin waves in the Damon-Eshbach configuration normally have positive group velocity [34]. However, it was already observed in the presence of a perpendicular magnetic anisotropy [20] and it finds a natural explanation here: The perpendicular magnetic anisotropy favors the out-of-plane component of the magnetization precession with respect to the in-plane one, which allows for a certain degree of dipolar field cancellation at sufficiently short length scale. Decreasing the field to 14 mT, i.e., about 2 mT above stripe nucleation, leads to a clear frequency decrease [Fig. 2(d)], which can be extrapolated to a perfect softening at (k_c, H_c). Let us now examine the spin-wave dispersion below nucleation. Symbols in Fig. 3(a) show the positions of the Brillouin light scattering peaks measured at 7 mT (see raw data in Fig. S5 in the Supplemental Material). We distinguish clearly two branches. The frequency of the bottom one decreases rapidly as a function of wave number down to an extrapolate $f \sim 0$ at k_c. The frequency of the top one decreases much slower and extrapolates to a value of about 3.5 GHz at k_c. To help interpret these observations, we have performed MUMAX3 finite-difference micromagnetic simulations [39] of spin-wave propagation. Figures 3(a)–3(c) show color plots of the amplitude spectral density obtained upon Fourier transforming the spatiotemporal evolution of the surface magnetization following a localized pulse excitation (see Supplemental Material [24]) for field values of 7, 10, and 11.7 mT, respectively. Right below nucleation [Fig. 3(c)], one distinguishes a secondary branch with a nonzero minimum frequency emerging from the characteristic $(k, f) = (k_c, 0)$ cusp. Upon reducing further the field, the minimum frequency of this secondary branch gradually increases, while the main branch remains soft [Fig. 3(b)]. These two branches account very well for the measured inelastic peak positions [Fig. 3(a)]. This phenomenology can be understood as the mesoscopic counterpart of the one occurring at the microscopic level for charge density waves [40] and incommensurate displacive phases [7] whose nucleation is also described by the softening of a dynamic mode which splits into amplitude and phase modes upon symmetry breaking. Figures 3(d) and 3(e) show maps of the out-of-plane component of the dynamic magnetization $m_y(x, y)$ at k_c for these two branches, together with the distribution of the transverse static magnetization, sketched as a vector plot. One clearly recognizes two similar patterns phase shifted by $\pi/2$. For the zero-frequency mode, the antinodes of the dynamic magnetization are aligned
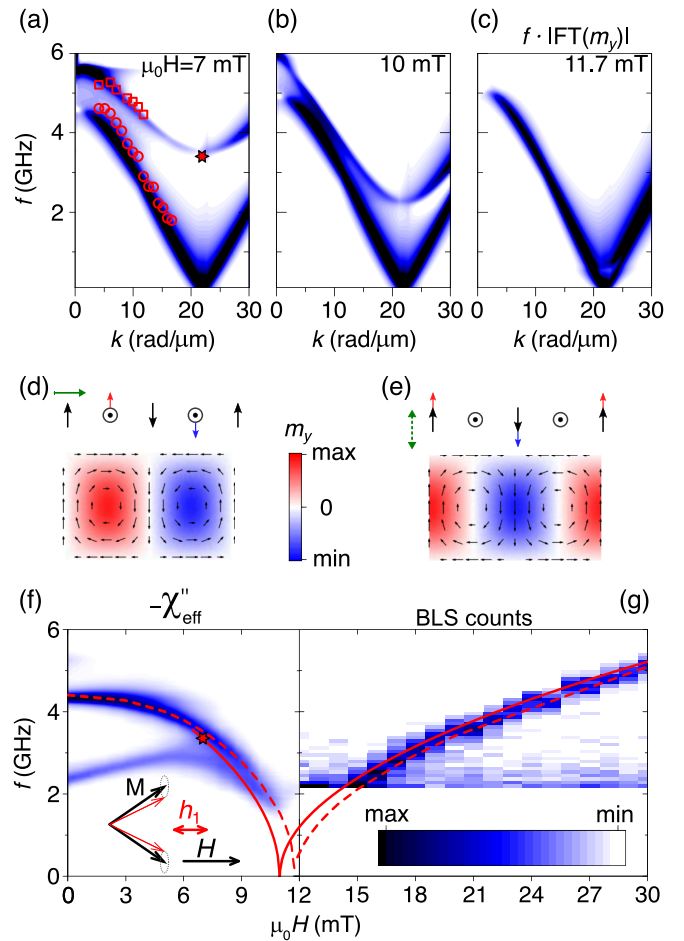
FIG. 3. (a)–(c) Color plot of the simulated spin-wave spectrum amplitude density as a function of wave vector and frequency, for a field of 7, 10, and 11.7 mT, respectively. In (a), the positions of the measured Brillouin light scattering peaks are reported as circles and squares and the Higgs mode frequency determined analytically is shown as a star. (d) Color plot of the distribution of the out-of-plane component of the dynamic magnetization for the Goldstone mode [$k = k_c$, $f = 0.1$ GHz in (b)]. The vector plot shows the distribution of the transverse magnetization of the underlying static stripe modulation. (e) Same for the Higgs mode [$k = k_c$, $f = 3.5$ GHz in (b)]. The green arrows sketch the motion of the stripe structure, namely a rigid displacement and an amplitude oscillation in (d) and (e), respectively. (f) Color plot of the microwave absorption measured in the stripe phase as a function of field and frequency, for the longitudinal pumping geometry sketched in the inset. (g) Color plot of the Brillouin light scattering intensity measured in the saturated phase as a function of field and frequency for a transferred wave vector $k_c = 21$ rad/μm. The solid and dashed lines in (f) and (g) show the soft/Higgs mode frequency extracted from our analytical approach (see details in the Supplemental Material [24] and Ref. [41] therein) and from micromagnetic simulations, respectively. The (min, max) values for color plots are (4,20), $(-1, -18) \times 10^{-3}$, and (100,300) for (a)–(c), (f), and (g), respectively.

with the nodes of the static distribution [Fig. 3(d)]. In contrast, for the nonzero-frequency mode, dynamic and static antinodes are aligned with each other [Fig. 3(e)]. The evolution with respect to the spectrum above saturation is explained as follows: The phase transition being second order, the overall spin-wave

spectrum changes smoothly upon stripe nucleation. The soft spin waves actually adapt in the form of intensity modulations in phase or in quadrature with respect to the nucleated texture.

We shall now identify these two types of modulations with the Goldstone and Higgs modes of the stripe texture. According to Fig. 1(a), in the low-symmetry phase, one should distinguish phase oscillations $\delta = \delta_0 + \delta_1 \cos(\omega t)$ and amplitude oscillations $|\psi| = \psi_0 + \psi_1 \cos(\omega t)$. As these time oscillations occur around an equilibrium which is oscillating in space (e.g., $M_y(x, 0) \propto \cos[k_c(x - \delta_0)]$), they correspond to nonzero wave-number spin waves. More precisely, the dynamic magnetization profiles (e.g., $\delta_1 \frac{\partial M_y}{\partial x}(x, 0) \propto \sin[k_c(x - \delta_0)]$ and $\psi_1 M_y(x, 0) \propto \cos[k_c(x - \delta_0)]$) can be interpreted as two standing-wave patterns formed by the interference between counterpropagating spin waves with $k = \pm k_c$ and a well-defined phase difference of 0 or $\pi/2$ with respect to the equilibrium modulation. This corresponds exactly to the modal distributions of Figs. 3(d) and 3(e), to be identified with the Goldstone and Higgs modes, respectively. The zero frequency of the former is associated with the translation invariance of the whole stripe texture: The total energy is exactly the same whatever the value of the lateral shift δ in Fig. 1(d), as already noticed by Ref. [20]. The nonzero frequency of the Higgs mode arises from the finite curvature of the energy potential along the radial direction. We can evaluate this frequency via a suitable extension of the description of the dynamics above saturation [7,10]. From the expression of the Landau potential, it can be shown that the positive curvature around the stable equilibrium value $\psi_0 = \sqrt{\frac{-a}{2b}}$ is related to the negative curvature around the unstable equilibrium value $\psi = 0$, namely $(\frac{\partial^2 E}{\partial |\psi|^2})_{\psi_0} = -2(\frac{\partial^2 E}{\partial |\psi|^2})_0$. Then, we can write the frequency of the amplitude mode as $\omega \propto \sqrt{\frac{\partial^2 E}{\partial |\psi|^2} \frac{\partial^2 E}{\partial \tau^2}}$, where $\frac{\partial^2 E}{\partial \tau^2}$ is a "kinetic" term accounting for the extra energy generated by magnetization precession (Fig. S3 in the Supplemental Material [24]). This is essentially a strong demagnetizing contribution [Fig. 2(a)] which does not depend on the subtle energy balance that governs nucleation. It can therefore be assumed to be the same at $|\psi| = 0$ and ψ_0. Accordingly, we obtain $\omega|_{\psi_0} = -i\sqrt{2}\omega|_0$, which allows us to relate the frequency of the Higgs mode in the low-symmetry phase to the growth rate of the unstable mode in a fictitious high-symmetry state below nucleation. Using the growth rate calculated from our spin-wave ansatz [bottom panel in Fig. 2(b)], we obtain the value shown as a star in Fig. 3(a), in good agreement with the numerical simulations.

To characterize directly the approach towards the critical point from both sides, we finally combine two techniques [Figs. 3(f) and 3(g)]. The mode softening in the saturated phase ($H > H_c$) is followed by Brillouin light scattering, placing ourselves exactly at k_c [Fig. 3(g)]. There, one distinguishes clearly a gradual drop which follows precisely the characteristic softening predicted for the precursor mode by our analytical approach (solid line) or by micromagnetic simulations (dashed line). This technique becomes less efficient in the stripe phase because of the dephasing induced by inhomogeneities of the stripe phase across the several tens of μm of the focal spot of the laser. This results in a sizable drop of the light scattering signal at high wave numbers [Fig. S5(b) in the Supplemental Material [24]]. Rather,

we resort to another technique able to probe the stripe texture in a scalar way [42] (i.e., regardless of the phase of the nucleated texture [6]), namely ferromagnetic resonance under longitudinal pumping. The measurement configuration is shown in the inset of Fig. 3(f). The film is placed on top of a broadband transmission line [see Fig. S6(a) in the Supplemental Material [24] and Ref. [43] within it for details], which generates a (mostly in-plane and homogeneous) microwave magnetic field $\boldsymbol{h}_1$, the static field $\boldsymbol{H}$ being oriented parallel to it. This can be viewed as an analog of the lattice depth modulation technique used in cold atom systems [9]: During a microwave cycle, the pumping field alternatively increases and decreases the total external field, which translates into an oscillation of the Zeeman energy and, in turn, into an oscillation of the amplitude of the order parameter. Figure 3(f) shows the imaginary part of the effective magnetic susceptibility χ_{eff} of the loaded transmission line (which is proportional to the microwave absorption coefficient) as a function of both the microwave frequency and the static field intensity. One recognizes clearly a strong absorption feature below H_c, with a frequency increasing from about 1.5 GHz, in good agreement with the frequency upturn predicted by our analytical approach (solid line) and simulations (dashed line) [44]. This absorption is associated to the excitation torque $\boldsymbol{M}(x, y) \times \boldsymbol{h}_1$ which is zero in the saturated state but increases gradually below nucleation due to the transverse static components of the stripe modulation ($\boldsymbol{M} \perp \boldsymbol{h}_1$). This allows us to shed light onto previous experiments of ferromagnetic resonance in stripe domains, traditionally interpreted in terms of distinct domain and domain-wall resonances [17–19,21]. Our analysis indicates that the mode probed by longitudinal pumping corresponds to a spin wave already present in the saturated state at $k = k_c$ and made accessible to a $k = 0$ experiment by a Bragg scattering process induced by the nucleated texture.

III. CONCLUSION

To conclude, we show that both the close-to-nucleation statics and the low-frequency dynamics of magnetic stripe domains are entirely determined by the specific behavior of flux-closure Damon-Eshbach spin waves around a certain wave vector k_c. The evolution of the whole spin-wave dispersion upon the high- to low-symmetry transition can be analyzed in universal terms invoking the softening of the low-frequency spin-wave branch, its freezing in the form of the translation-symmetry-breaking static stripe modulation, and its subsequent splitting into a Goldstone and a Higgs branch. The identified intimate relationship between the statics and the dynamics of a magnetic texture is a generic feature that could be taken advantage of in future developments of magnonics [22,45–48]. More importantly, the described system constitutes a particularly simple and explicit implementation of the dynamics around symmetry-breaking phase transitions, paving the way for further exploration, including time-resolved imaging studies, extension to the nonlinear regime, or the quest for a possible Higgs-Anderson mechanism for magnons.

M.Gr., D. S., Y.H., and M.B. designed the experiments; M.H. fabricated the magnetic films; K.A. and D.L. performed magnetometry and magnetic imaging; M.Ge. performed Brillouin light scattering measurements; M.Gr. performed ferromagnetic measurements and analyzed the experimental data, with the help of M.Ge., P.P., and M.B.; M.Gr. and M.B. developed the analytical model; D.S. performed the micromagnetic simulations with the help of Y.H. and M.Gr.; M.Gr. and M.B. wrote the manuscript with the help of all authors.

[1] D. Pekker and C. M. Varma, Amplitude/Higgs modes in condensed matter physics, Annu. Rev. Condens. Matter Phys. **6**, 269-297 (2015).

[2] R. Currat, Neutron investigation of modulated crystals, Phys. B: Condens. Matter **156**, 1 (1989).

[3] L. Landau and E. Lifshitz, *Statistical Physics* (Mir, Moscow, 1964).

[4] P. Higgs, Nobel Lecture: Evading the Goldstone theorem, Rev. Mod. Phys. **86**, 851 (2014).

[5] F. Englert, Nobel Lecture: The BEH mechanism and its scalar boson, Rev. Mod. Phys. **86**, 843 (2014).

[6] D. Podolsky, A. Auerbach, and D. P. Arovas, Visibility of the amplitude (Higgs) mode in condensed matter, Phys. Rev. B **84**, 174522 (2011).

[7] P. Launois, F. Moussa, M. H. Lemée-Cailleau, and H. Cailleau, Phase and amplitude modes of the $n = 4$ incommensurate phase II of biphenyl: Neutron scattering experiments and theoretical results, Phys. Rev. B **40**, 5042 (1989).

[8] C. Rüegg, B. Normand, M. Matsumoto, A. Furrer, D. F. McMorrow, K. W. Krämer, H.-U. Güdel, S. N. Gvasaliya, H. Mutka, and M. Boehm, Quantum Magnets under Pressure: Controlling Elementary Excitations in $TlCuCl_3$, Phys. Rev. Lett. **100**, 205701 (2008).

[9] M. Endres, T. Fukuhara, D. Pekker, M. Cheneau, P. Schauss, C. Gross, E. Demler, S. Kuhr, and I. Bloch, The "Higgs" amplitude mode at the two-dimensional superfluid/Mott insulator transition, Nature (London) **487**, 454 (2012).

[10] J. Léonard, A. Morales, P. Zupancic, T. Donner, and T. Esslinger, Monitoring and manipulating Higgs and Goldstone modes in a supersolid quantum gas, Science **358**, 1415 (2017).

[11] A. Hubert and R. Schäfer, *Magnetic Domains* (Springer, Berlin, 1998).

[12] L. Landau and E. Lifshitz, On the theory of the dispersion of magnetic permeability in ferromagnetic bodies, Phys. Z. Sowjetunion **8**, 153 (1935).

[13] M. W. Müller, Distribution of the magnetization in a ferromagnet, Phys. Rev. **122**, 1485 (1961).

[14] W. F. Brown, Jr., Rigorous calculation of the nucleation field in a ferromagnetic film or plate, Phys. Rev. **124**, 1348 (1961).

[15] J. R. Spain, Dense-banded domain structure in "rotatable anisotropy" permalloy films, Appl. Phys. Lett. **3**, 208 (1963).

[16] N. Saito, H. Fujiwara, and Y. Sugita, A new type of magnetic domain in thin Ni-Fe films, J. Phys. Soc. Jpn. **19**, 421 (1964).

[17] B. Lührmann, H. Dötsch, and S. Sure, High-frequency excitations of stripe-domain lattices in magnetic garnet films, Appl. Phys. A **57**, 553 (1993).

[18] U. Ebels, L. Buda, K. Ounadjela, and P. E. Wigen, Ferromagnetic resonance excitation of two-dimensional wall structures in magnetic stripe domains, Phys. Rev. B **63**, 174437 (2001).

[19] N. Vukadinovic, M. Labrune, J. Ben Youssef, A. Marty, J. C. Toussaint, and H. Le Gall, Ferromagnetic resonance spectra in a weak stripe domain structure, Phys. Rev. B **65**, 054403 (2001).

[20] C. Banerjee, P. Gruszecki, J. W. Klos, O. Hellwig, M. Krawczyk, and A. Barman, Magnonic band structure in a Co/Pd stripe domain system investigated by Brillouin light scattering and micromagnetic simulations, Phys. Rev. B **96**, 024421 (2017).

[21] I. S. Camara, S. Tacchi, L.-C. Garnier, M. Eddrief, F. Fortuna, G. Carlotti, and M. Marangolo, Magnetization dynamics of weak stripe domains in Fe-N thin films: A multitechnique complementary approach, J. Phys.: Condens. Matter **29**, 465803 (2017).

[22] C. Liu, S. Wu, J. Zhang, J. Chen, J. Ding, J. Ma, Y. Zhang, Y. Sun, S. Tu, H. Wang, P. Liu, C. Li, Y. Jiang, P. Gao, D. Yu, J. Xiao, Re. Duine, M. Wu, C.-W. Nan, J. Zhang, and H. Yu, Current-controlled propagation of spin waves in antiparallel, coupled domains, Nat. Nanotechnol. **14**, 691 (2019).

[23] K. Ait Oukaci, D. Lacour, D. Stoeffler, B. Sarpi, F. Montaigne, R. Belkhou, and M. Hehn, Weak Stripe Angle Determination by Quantitative x-ray Magnetic Microscopy, Phys. Rev. Appl. **14**, 024083 (2020).

[24] See Supplemental Material at http://link.aps.org/supplemental/10.1103/PhysRevB.105.094444 for additional information about materials and methods.

[25] P. Talagala, P. S. Fodor, D. Haddad, R. Naik, L. E. Wenger, P. P. Vaishnava, V. M. Naik, Determination of magnetic exchange stiffness and surface anisotropy constants in epitaxial $Ni_{1−x}Co_x$ (001) films, Phys. Rev. B **66**, 144426 (2002).

[26] K. A. Oukaci, Periodic magnetic domain structures for channeled spin waves propagation, thesis, Université de Lorraine, Nancy, 2021.

[27] G. Suran, M. Naili, H. Niedoba, F. Machizaud, O. Acher, and D. Pain, Magnetic and structural properties of Co-rich CoFeZr amorphous thin films, J. Magn. Magn. Mater. **192**, 443 (1999).

[28] A. Hubert, Stray-field-free magnetization configurations, Phys. Status Solidi **32**, 519 (1969).

[29] M. Grassi, Spin waves in inhomogeneous magnetization distributions, thesis, Université de Strasbourg, 2021.

[30] G. Asti, M. Ghidini, M. Mulazzi, R. Pellicelli, M. Solzi, K. Chesnel, and A. Marty, Nucleation of weak stripe domains: Determination of exchange and anisotropy thermal variation, Phys. Rev. B **76**, 094414 (2007).

[31] A. G. Gurevich and G. A. Melkov, *Magnetization Oscillations and Waves* (CRC Press, Boca Raton, FL, 1996).

[32] M. Grassi, M. Geilen, D. Louis, M. Mohseni, T. Brächer, M. Hehn, D. Stoeffler, M. Bailleul, P. Pirro, and Y. Henry, Slow-Wave-Based Nanomagnonic Diode, Phys. Rev. Appl. **14**, 024047 (2020).

[33] Y. Henry, O. Gladii, and M. Bailleul, Propagating spin-wave normal modes: A dynamic matrix approach using plane-wave demagnetizing tensors, arXiv:1611.06153.

[34] R. W. Damon and J. R. Eshbach, Magnetostatic modes of a ferromagnet slab, J. Phys. Chem. Solids **19**, 308 (1961).

[35] B. A. Kalinikos and A. N. Slavin, Theory of dipole-exchange spin wave spectrum for ferromagnetic films with mixed exchange boundary conditions, J. Phys. C: Solid State Phys. **19**, 7013 (1986).

[36] G. Leaf, H. Kaper, M. Yan, V. Novosad, P. Vavassori, R. E. Camley, and M. Grimsditch, Dynamic Origin of Stripe Domains, Phys. Rev. Lett. **96**, 017201 (2006).

[37] T. Sebastian, K. Schultheiss, B. Obry, B. Hillebrands, and H. Schultheiss, Micro-focused Brillouin light scattering: Imaging spin waves at the nanoscale, Front. Phys. **3**, 35 (2015).

[38] P. Grünberg, C. M. Mayr, W. Vach, and M. Grimsditch, Determination of magnetic parameters by means of Brillouin scattering. Examples: Fe, Ni, $Ni_{0.8}Fe_{0.2}$, J. Magn. Magn. Mater. **28**, 319 (1982).

[39] A. Vansteenkiste, J. Leliaert, M. Dvornik, M. Helsen, F. Garcia-Sanchez, and V. B. Waeyenberge, The design and verification of mumax3, AIP Adv. **4**, 107133 (2014).

[40] J. P. Pouget, B. Hennion, C. Escribe-Filippini, and M. Sato, Neutron-scattering investigations of the Kohn anomaly and of the phase and amplitude charge-density-wave excitations of the blue bronze $K_{0.3}MoO_3$, Phys. Rev. B **43**, 8421 (1991).

[41] H. Y. Yuan and R. A. Duine, Universal field dependence of magnetic resonance near zero frequency, Phys. Rev. B **103**, 134440 (2021).

[42] In this context scalar means that the probe is not sensitive to the phase of the texture. This is in contrast with a vectorial probe which measures a projection along a certain phase realization [6], as Brillouin light scattering which involves a well-defined phase over the whole laser beam.

[43] C. Bilzer, T. Devolder, P. Crozat, and C. Chappert, Vector network analyzer ferromagnetic resonance of thin films on coplanar waveguides: Comparison of different evaluation methods, J. Appl. Phys. **101**, 074505 (2007).

[44] The additional absorption line in Fig. 3(f) is discussed in the Supplemental Material [24].

[45] H. Yu, J. Xiao, and H. Schultheiss, Magnetic texture based magnonics, Phys. Rep. **905**, 1 (2021).

[46] K. Wagner, A. Kákay, K. Schultheiss, H. Henschke, T. Sebastian, and H. Schultheiss, Magnetic domain walls as reconfigurable spin-wave nanochannels, Nat. Nanotechnol. **11**, 432 (2016).

[47] V. Sluka, T. Schneider, R. A. Gallardo, A. Kákay, M. Weigand, T. Warnatz, R. Mattheis, A. Roldán-Molina, P. Landeros, V. Tiberkevich, A. Slavin, G. Schütz, A. Erbe, A. Deac, J. Lindner, J. Raabe, J. Fassbender, and S. Wintz, Emission and propagation of 1D and 2D spin waves with nanoscale wavelengths in anisotropic spin textures, Nat. Nanotechnol. **14**, 328 (2019).

[48] J. Han, P. Zhang, J. T. Hou, S. A. Siddiqui, and L. Liu, Mutual control of coherent spin waves and magnetic domain walls in a magnonic device, Science **366**, 1121 (2019).